

# Predicting Mode-I/II fracture toughness and crack growth in diboride ceramics via machine-learning potentials

Shuyao Lin<sup>1,2\*</sup>, Zhuo Chen<sup>3</sup>, Rebecca Janknecht<sup>1</sup>, Zaoli Zhang<sup>3</sup>, Lars Hultman<sup>2,4</sup>, Paul H. Mayrhofer<sup>1</sup>, Nikola Koutná<sup>1,2</sup>, and Davide G. Sangiovanni<sup>2</sup>

<sup>1</sup>Technische Universität Wien, Institute of Materials Science and Technology, Vienna, A-1060, Austria

<sup>2</sup>Linköping University, Department of Physics, Chemistry, and Biology (IFM), Linköping, SE-58183, Sweden

<sup>3</sup>Austrian Academy of Sciences, Erich Schmid Institute of Materials Science, Leoben, A-8700, Austria

<sup>4</sup>Center for Plasma and Thin Film Technologies, Ming Chi University of Technology, New Taipei City, 24301, Taiwan

\*shuyao.lin@tuwien.ac.at

## ABSTRACT

Fracture toughness and strength are critical for structural ceramics, which are prone to brittle failure. However, accurately characterizing these properties is challenging, especially for thin films on substrates. In-situ microscopy often fails to resolve crack initiation, while fractured samples provide limited insight into fracture modes and crack paths. Here, we employ stress intensity factor ( $K$ ) controlled atomistic simulations of fracture to characterize the crack-initiation properties of hard but brittle diboride ceramics. Our molecular statics calculations are based on moment-tensor machine-learning interatomic potentials (MLIPs) trained on *ab initio* information collected for a variety of atomistic environments.  $\text{TMB}_2$  (TM=Ti, Zr, Hf) lattice models with six distinct atomically-sharp crack geometries subjected to Mode-I (opening) and/or Mode-II (sliding) deformation serve as platforms to illustrate the capability of the approach. The Mode-I initiation toughness  $K_{Ic}$  and fracture strength  $\sigma_f$ —within ranges 1.8-2.9  $\text{MPa}\cdot\sqrt{m}$  and 1.6-2.4 GPa—are extrapolated at the macroscale limit by fitting the results of finite (up to  $10^6$  atoms) cracked plate models with constitutive scaling relations. Our simulations show that most diboride lattice models fail by extension of the native crack. However, crack-deflection on the  $(1\bar{1}01)$  plane is observed for the  $(10\bar{1}0)[\bar{1}2\bar{1}0]$  crystal geometry. As exemplified by  $\text{TiB}_2$ , varying Mode-I/II loading ratios have little influence on crack propagation paths, which overall occurs by decohesion of low-energy fracture planes or combined sliding. Our predictions are supported by cube-corner nanoindentation on  $\text{TiB}_2$  samples along the  $[0001]$  direction, revealing the same fracture plane as observed in simulations and a  $K_{Ic}$  of 3.1  $\text{MPa}\cdot\sqrt{m}$ . Our work demonstrates the possibility of predicting orientation-dependent fracture behaviors in hard ceramics, highlighting the effectiveness of machine-learning-potential simulations.

**Keywords:** Transition metal diborides; Machine-Learning interatomic potentials; Fracture toughness; Molecular statics

## Introduction

Fracture mechanics roots in Griffith's pioneering work during the 1920s<sup>1</sup>. Griffith understood that strong but brittle solids, such as glass, break at stress levels much lower than their theoretical strength due to microstructural imperfections which, acting as stress concentrators, cause fracture initiation. His investigations led to the conclusion that the extension of native cracks occurs if the elastic-strain energy released during crack-growth exceeds the formation energy of new crack surfaces. Thirty years later, Irwin<sup>2</sup> broadened the energy-balance approach proposed by Griffith to account for dissipative non-linear responses (e.g., plastic deformation in metals). Irwin also introduced the concept of the stress intensity factor,  $K$ , quantifying the stress state near the crack tip. Furthermore, he categorized fracture modes into three distinct types—Mode-I (opening), Mode-II (sliding), and Mode-III (tearing)—where the conditions for crack propagation are dictated by critical values  $K_{Ic}$ ,  $K_{IIc}$ , and  $K_{IIIc}$ .

The critical stress intensity factor  $K_{Ic}$  is recognized as the

most practically significant. The term  $K_{Ic}$  is often referred to as the material's fracture toughness, as fracture in solids generally initiates at structural flaws under tension. The  $K_{Ic}$  is a property measured through standardized tests (see, e.g., Refs.<sup>3-7</sup>), which involve introducing a crack into a sample and applying a controlled load or displacement to determine the conditions leading to fracture. In general, the reproducibility of measured  $K_{Ic}$  values strongly depends on the sample's structural features and density of crystallographic defects<sup>8-14</sup>. Additionally, traditional fracture toughness tests cannot resolve nanoscale processes responsible for fracture initiation. The limitations of experimental techniques become even more evident when it comes to studying thin-film samples, due to the small sizes involved and substrate effects<sup>15</sup>. Hence, fundamental understanding and characterization of materials' fracture would necessitate complementing mechanical testing and/or state-of-the-art in-situ imaging<sup>16,17</sup> with atomistic simulations of crack behavior during loading.

Machine-learning interatomic potentials (MLIPs) can offer detailed atomic-scale understanding of materials' fracture initiation and accurate evaluation of fracture properties. Although the reliability and quality of MLIP-based simulations

is dependent on the underlying *ab initio* training set<sup>18–22</sup>, MLIPs are systematically improvable force fields<sup>23,24 25–27</sup> that can achieve accuracy rivaling that of density functional theory (DFT) calculations but with up to  $10^5$  times higher computational efficiency. We have recently proposed an MLIP training workflow and a validation standard<sup>28</sup> to reproduce the elastic and plastic properties of bulk ceramic lattices (free of extended crystallographic defects in the unstrained state) predicted by *ab initio* molecular dynamics (MD). Our MLIP-based MD simulations allowed investigating the variations of theoretical strength values as a function of the supercell size and the anisotropy of lattice slip and fracture processes during tensile and shear elongation at room as well as elevated temperatures. The training and validation strategy presented in Refs.<sup>28–30</sup> lay the foundations to this work.

Here we use MLIPs in *K*-controlled atomistic simulations of fracture to investigate the properties of Group-IV transition-metal diborides,  $\text{TMB}_2$ :s (TM=Ti, Zr, Hf). As most ceramics,  $\text{TMB}_2$ :s are prone to crack without yielding, but exhibit ultra-high thermal stability<sup>31</sup>, exceptionally high hardness<sup>32</sup>, corrosion resistance, and excellent thermal and electrical conductivity<sup>33</sup>. Unlike other hard ceramic protective coatings (e.g. nitrides and carbides, for which the fracture properties have been characterized relatively thoroughly<sup>34–39</sup>), information on the toughness and strength available in the literature for  $\text{TMB}_2$ :s is sparse<sup>40–42</sup>. An experimental characterization of the fracture resistance of diboride films is further complicated by largely varying degrees of  $\text{TMB}_{1.53–2.72}$  stoichiometry which, together with a typically high density of crystallographic defects<sup>43,44</sup>, constitutes an additional hurdle to understanding the structure/property relationship in this class of materials<sup>45</sup>. The limitations of the experiments provide further motivation to use MLIPs to determine the crack behavior in diboride systems.

## Results and discussion

### 1 MLIP validation and theoretical strengths of defect-free crystals

The moment tensor potential (MTP) framework<sup>27</sup> is employed to train machine-learning interatomic potentials (MLIPs) for the Group-IV transition metal diborides ( $\text{TiB}_2$ ,  $\text{ZrB}_2$ ,  $\text{HfB}_2$ ; all crystallizing in the  $\alpha/\text{AlB}_2$ -type phase<sup>51</sup>), using datasets from *ab initio* MD simulations. Training and validation errors, quantified by the residual mean square error (RMSE), remain below 8 meV/atom for energies, 0.24 eV/Å for forces, and 0.6 GPa for stresses, as detailed in the Supplementary Material. Prior to simulations on defective diboride crystals under loading, the reliability of the here-developed MLIPs is showcased by the comparison with DFT-calculated properties as well as with room-temperature *ab initio* MD tensile tests.

Tab. 1 presents the results obtained by MLIP-based molecular statics simulations in the context with own reference DFT calculations as well as DFT data from other studies. Although trained mainly on finite-temperature *ab initio* MD snapshots,

our MLIPs reproduce 0 K *ab initio* lattice parameters ( $a$ ,  $c$ ), elastic constants ( $C_{ij}$ ), and surface energies ( $E_{\text{surf}}$ ) satisfactorily well. Note that DFT and *ab initio* MD calculations of this work are carried out using the same accuracy parameters (see the **Methods**). The deviations in lattice parameters are below 0.7%, while the  $C_{11}$ ,  $C_{33}$ , and  $C_{44}$  elastic constants, as well as the polycrystalline bulk ( $B$ ), shear ( $G$ ) and Young’s moduli ( $E$ ) differ by less than 10% from the corresponding DFT values. For  $C_{ij}$ ,  $i \neq j$ , elastic constants, the deviations are generally below 20%. The differences between *ab initio* and MLIP-calculated surface energies are lower than 6.5%. Our results are also consistent with those from other DFT studies.

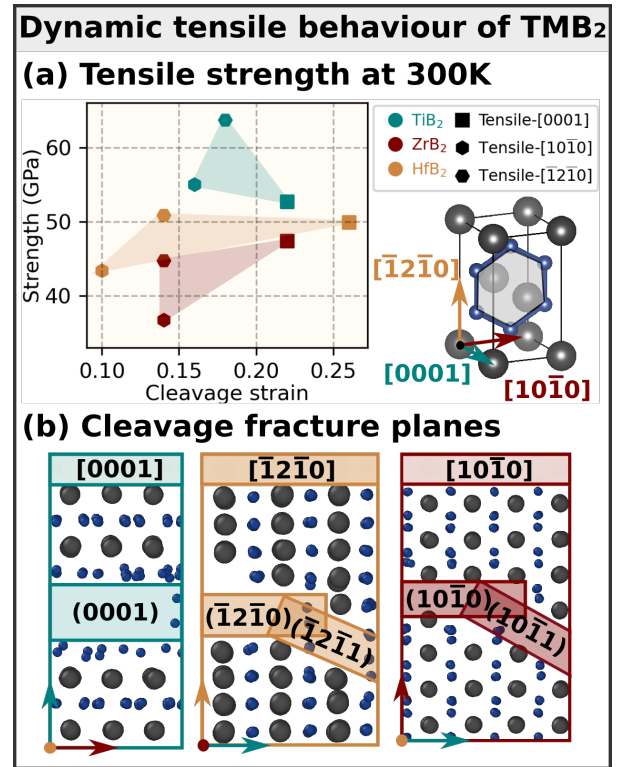


**Figure 1.** Uniaxial tensile simulations at 300 K via MLIP-assisted molecular dynamics (ML-MD). (a) Maximum stress (theoretical tensile strength) sustained by  $\text{TMB}_2$ :s, (TM=Ti, Zr, Hf) during uniaxial tensile deformation along  $[0001]$  (square),  $[10\bar{1}0]$  (vertical hexagon), and  $[\bar{1}2\bar{1}0]$  (horizontal hexagon) directions. (b) Cleavage fracture after reaching the maximum stress point, with plane recognition. The side image in (a) shows the atomic structure of the  $\alpha$ -phase, including orthogonalized axis notation. The shadowed boron hexagonal plane represents the basal plane.

In our previous work<sup>28,29</sup>, we have thoroughly tested the reliability of  $\text{TiB}_2$ -MLIP against finite-temperature *ab initio* MD tensile and shear simulations, considering loading geometries characterized by low-index crystallographic directions and planes. Furthermore, transferability to tensile and shear tests beyond DFT length scales has been shown for initially defect-free single crystal  $\text{TiB}_2$  using the concept of extrapolation grade. As the MLIPs for  $\text{HfB}_2$  and  $\text{ZrB}_2$  in this work were trained using the same strategy, we do not repeat all validation

**Table 1. Validation against 0 K DFT calculations** of lattice parameters ( $a$ ,  $c$  in Å), elastic constants ( $C_{ij}$ , in GPa), and polycrystalline moduli (Young’s modulus,  $E$ , bulk modulus,  $B$ , shear modulus,  $G$ , in GPa). Additionally, relaxed surface energies  $E_{\text{surf}}$  of (0001), (10 $\bar{1}$ 0), and ( $\bar{1}$ 2 $\bar{1}$ 0) (in J/m<sup>2</sup>) are provided for both DFT and ML-MS calculations. Reference values from the literature are listed for each material.

TMB <sub>2</sub>	LC (Å)		Elastic constants (GPa)							Surface energy (J/m <sup>2</sup> )			Reference	
	$a$	$c$	$C_{11}$	$C_{33}$	$C_{44}$	$C_{12}$	$C_{13}$	$E$	$B$	$G$	(0001)	(10 $\bar{1}$ 0)		( $\bar{1}$ 2 $\bar{1}$ 0)
TiB <sub>2</sub>	3.027	3.213	654	464	259	76	115	580	263	256	3.80	3.98	3.42	This work (DFT)
	3.030	3.204	636	441	272	61	92	576	242	261	3.80	4.12	3.57	This work (ML-MS)
	3.029	3.219	656	461	259	65	98	582 <sup>I</sup>	253 <sup>I</sup>	261 <sup>I</sup>	/	/	/	Ref. <sup>46</sup>
	/	/	660	464	255	60	96	583 <sup>I</sup>	250	258	4.20 <sup>II</sup>	4.10 <sup>II</sup>	/	Ref. <sup>47</sup>
	3.029	3.219	/	/	/	/	/	/	/	/	4.21	4.19	/	Ref. <sup>48</sup>
ZrB <sub>2</sub>	3.180	3.545	539	422	270	52	109	523	226	235	3.86	4.54	3.83	This work (DFT)
	3.167	3.531	551	427	248	54	118	517	234	228	3.61	4.38	3.57	This work (ML-MS)
	3.168	3.536	555	436	254	62	119	524	238	231	/	/	/	Ref. <sup>46</sup>
	/	/	539	420	238	60	116	502 <sup>I</sup>	231	218	3.85 <sup>II</sup>	4.45 <sup>II</sup>	/	Ref. <sup>47</sup>
	3.168	3.536	/	/	/	/	/	/	/	/	3.91	4.33	/	Ref. <sup>49</sup>
HfB <sub>2</sub>	3.149	3.480	602	432	309	57	105	580	238	266	3.88	4.53	4.07	This work (DFT)
	3.127	3.473	604	473	271	70	137	565	263	248	3.53	4.51	3.83	This work (ML-MS)
	3.165	3.512	584	457	257	98	135	544	253	238	/	/	/	Ref. <sup>46</sup>
	/	/	588	448	248	89	138	533 <sup>I</sup>	260	227	3.80 <sup>II</sup>	4.35 <sup>II</sup>	/	Ref. <sup>47</sup>
	3.163	3.515	602	452	258	78	137	550	260	239	/	/	/	Ref. <sup>50</sup>

<sup>I</sup>: Calculated based on the reference data.

<sup>II</sup>: Approximate value read from the presented figures.

steps (please see the Supplementary Material). Overall, the results obtained with our force fields closely match those of the underlying *ab initio* MD training configurations describing mechanical response within the elastic regime until fracture.

Fig. 1 depicts the theoretical tensile strength and the corresponding fracture strain subject to uniaxial tensile strain along the [0001], [10 $\bar{1}$ 0], [ $\bar{1}$ 2 $\bar{1}$ 0] direction, respectively, allowing to assess the degree of anisotropy in response to elongation. Irrespective of the loading direction, TiB<sub>2</sub> is the strongest among the studied systems, followed by HfB<sub>2</sub> and ZrB<sub>2</sub> (Fig. 1-(b)). All three materials sustain the largest strain along the [0001] direction. According to Fig. 1-(b), the three simulated loading scenarios lead to brittle cleavage along the basal, prismatic, or pyramidal planes, consistently for TM=Ti, Zr, Hf, i.e., the failure mechanisms remain independent of the TM. For instance, the [0001] tensile loading causes a fracture along the (0001) plane for TiB<sub>2</sub>, ZrB<sub>2</sub>, as well as HfB<sub>2</sub>, only the maximum stress withstood by each diboride is different.

## 2 Cracked-plate lattice models for simulations of fracture

The mechanical properties of diborides are calculated by  $K$ -controlled loading of plate lattice models containing an atomically sharp crack. The fracture-initiation strength and fracture-initiation toughness are obtained at the  $K$  value for which the crack tip has advanced by two percent of the model width. The calculations are repeated as a function of the plate area, so that the fracture initiation toughness and fracture initiation strength can be extrapolated at the macroscale limit by constitutive scaling relations, as done in Ref.<sup>52</sup>. Below, the crack plane and crack line of a supercell are indicated as

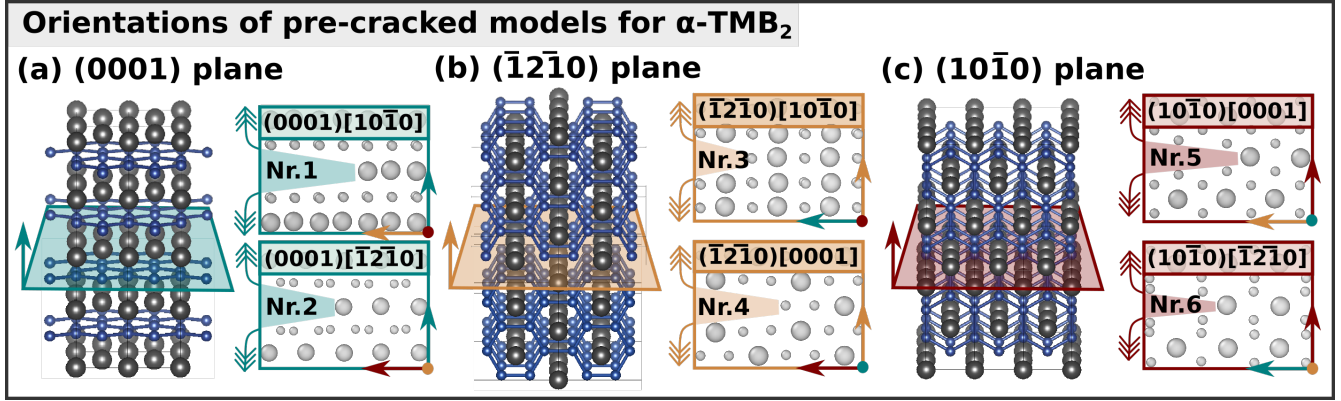
( $hklm$ )[ $h'k'l'm'$ ], where  $h$ ,  $k$ ,  $l$ , and  $m$  and their primes are crystallographic indexes of a hexagonal lattice.

Fig. 2 illustrates six crack geometries characterized by low-index planes and crack-line directions for hexagonal  $\alpha$ -structured TMB<sub>2</sub>s. Among them, the orientations ( $\bar{1}$ 2 $\bar{1}$ 0)-[10 $\bar{1}$ 0] and (10 $\bar{1}$ 0)-[ $\bar{1}$ 2 $\bar{1}$ 0] have the crack plane orthogonal to the [0001] axis. Thus, simulation results of fracture properties obtained for model Nr.1 and Nr.2 in Fig. 2 are of the highest relevance for comparison with experimental testing: since the [0001] is the typical growth direction of TMB<sub>2</sub> thin-film coatings, experimental toughness measurements induce crack formation normal to the (0001) plane.

## 3 Mode-I loading (crack opening): comparison of different TMB<sub>2</sub>s

In  $K$ -controlled simulations, the stress-intensity factor is incremented sequentially to identify stress conditions corresponding to the onset of crack growth. The bond-breaking behavior at different stages of pure Mode-I loading—simulated by ML-MS using our MLIPs—are shown in Fig. 3, depicting TMB<sub>2</sub> models with crack-plane and crack-line directions defined in Fig. 2. Specifically, we visualize the atomic configuration before, immediately after, and far beyond  $K_I$  has reached the critical value,  $K_{Ic}$ .

For geometries based on the (0001) plane (Fig. 2-(a)), the B–TM bonds consistently break first, while for those based on the ( $\bar{1}$ 2 $\bar{1}$ 0) (Fig. 2-(b)) and (10 $\bar{1}$ 0) (Fig. 2-(c)) planes, the B–B bonds are the first to break. During the Mode-I opening process, as  $K_I$  increases ( $K_I \leq K_{Ic}$ ), stress becomes increasingly concentrated at the atom located at the crack tip. Upon reaching  $K_{Ic}$ , the corresponding bond breaks. Typically, only



**Figure 2.** Possible Mode-I loading geometries in the hexagonal  $\alpha$ -structured diborides (considering orthogonalized supercells). (a) (0001) crack surface with  $[10\bar{1}0]$  (up, *Nr.1*) and  $[\bar{1}2\bar{1}0]$  (down, *Nr.2*) crack-front directions. (b)  $(\bar{1}\bar{2}\bar{1}0)$  crack surface with  $[10\bar{1}0]$  (up, *Nr.3*) and  $[0001]$  (down, *Nr.4*) crack-front directions. (c)  $(10\bar{1}0)$  crack surface with  $[0001]$  (up, *Nr.5*) and  $[\bar{1}2\bar{1}0]$  (down, *Nr.6*) crack-front directions.

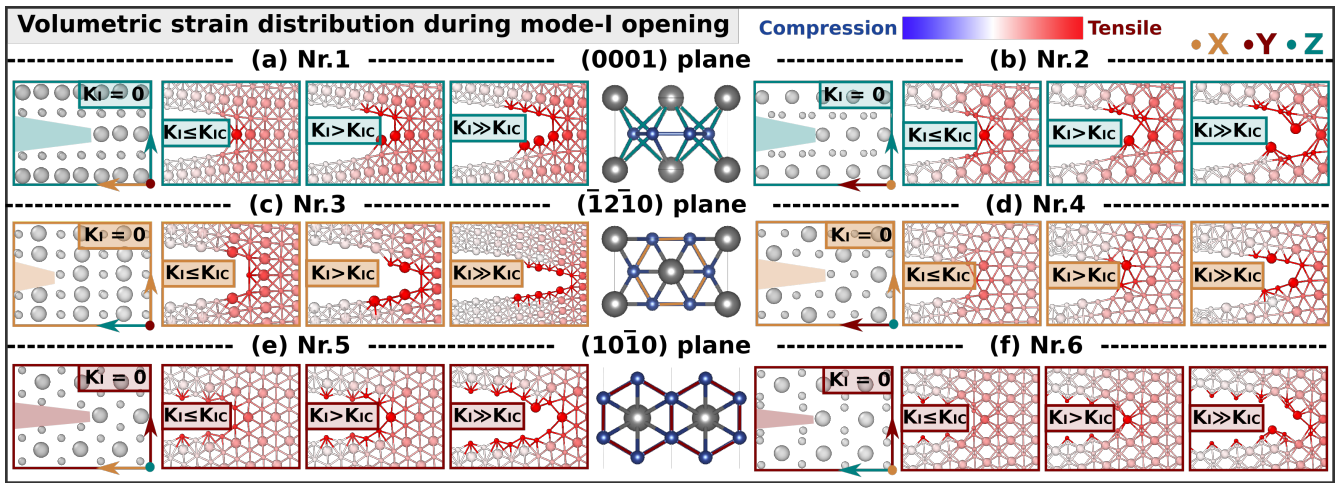


**Figure 3.** Bond breakage and volumetric strain distribution subject to Mode-I loading as a function of stress intensity: before, shortly after, and well after reaching the  $K_{Ic}$  point for different crack surfaces: (a, b) (0001), (c, d)  $(\bar{1}\bar{2}\bar{1}0)$ , and (e, f)  $(10\bar{1}0)$  planes. The first bond breakage occurs along the TM–B bond in (a, b), while in the other cases, the initial crack propagates along B–B bonds. The snapshots illustrate volumetric strain. For  $K_I = 0$ , all atoms appear in gray, while under increasing tensile, stress-responsive atoms turn red.

**Table 2.** Mode-I fracture toughness ( $K_{Ic}^\infty$ ) and Griffith fracture toughness ( $K_{Ic}^G$ ). The former is obtained from  $K$ -controlled static Mode-I simulations, while the latter is derived from unrelaxed surface energy ( $E_{surf}^{un}$ ) in ML-MS calculations. Additionally, the converged maximum stress values ( $\sigma_{max}^\infty$ ) are also compared. All converged values are presented with standard deviations, calculated as described in Ref.<sup>53</sup>.

Geometry	TiB <sub>2</sub>			ZrB <sub>2</sub>			HfB <sub>2</sub>		
	$K_{Ic}^\infty$ (MPa· $\sqrt{m}$ )	$K_{Ic}^G$ (MPa· $\sqrt{m}$ )	$\sigma_{max}^\infty$ (GPa)	$K_{Ic}^\infty$ (MPa· $\sqrt{m}$ )	$K_{Ic}^G$ (MPa· $\sqrt{m}$ )	$\sigma_{max}^\infty$ (GPa)	$K_{Ic}^\infty$ (MPa· $\sqrt{m}$ )	$K_{Ic}^G$ (MPa· $\sqrt{m}$ )	$\sigma_{max}^\infty$ (GPa)
(0001)[ $10\bar{1}0$ ] ( <i>Nr.1</i> )	1.81 ± 0.03	2.02	2.00 ± 0.77	2.03 ± 0.04	1.86	1.83 ± 0.65	2.75 ± 0.02	1.93	2.02 ± 0.64
(0001)[ $\bar{1}2\bar{1}0$ ] ( <i>Nr.2</i> )	2.35 ± 0.03	2.20	1.97 ± 0.49	2.08 ± 0.02	1.98	1.89 ± 0.22	2.89 ± 0.02	2.05	2.04 ± 0.31
(0001)	$E_{surf}^{un}$ : 4.02 (J/m <sup>2</sup> )			$E_{surf}^{un}$ : 3.68 (J/m <sup>2</sup> )			$E_{surf}^{un}$ : 3.61 (J/m <sup>2</sup> )		
( $\bar{1}\bar{2}\bar{1}0$ )[ $10\bar{1}0$ ] ( <i>Nr.3</i> )	2.24 ± 0.02	2.37	2.24 ± 0.63	1.74 ± 0.02	2.18	2.21 ± 0.68	2.01 ± 0.02	2.20	2.27 ± 0.61
( $\bar{1}\bar{2}\bar{1}0$ )[0001] ( <i>Nr.4</i> )	1.88 ± 0.02	2.29	2.22 ± 0.67	1.84 ± 0.02	2.15	1.75 ± 0.29	2.25 ± 0.05	2.18	1.61 ± 0.54
( $\bar{1}\bar{2}\bar{1}0$ )	$E_{surf}^{un}$ : 4.36 (J/m <sup>2</sup> )			$E_{surf}^{un}$ : 4.33 (J/m <sup>2</sup> )			$E_{surf}^{un}$ : 4.07 (J/m <sup>2</sup> )		
( $10\bar{1}0$ )[0001] ( <i>Nr.5</i> )	2.25 ± 0.02	2.24	2.26 ± 0.69	1.74 ± 0.02	2.04	2.21 ± 0.68	2.74 ± 0.03	2.22	2.36 ± 0.47
( $10\bar{1}0$ )[ $\bar{1}2\bar{1}0$ ] ( <i>Nr.6</i> )	2.24 ± 0.02	2.16	1.97 ± 0.60	1.93 ± 0.02	2.01	2.11 ± 0.33	2.25 ± 0.02	2.20	2.26 ± 0.34
( $10\bar{1}0$ )	$E_{surf}^{un}$ : 3.88 (J/m <sup>2</sup> )			$E_{surf}^{un}$ : 3.81 (J/m <sup>2</sup> )			$E_{surf}^{un}$ : 4.15 (J/m <sup>2</sup> )		

one bond breaks at this stage, but simultaneous breaking of multiple bonds is also possible, as observed in *Nr.3* (Fig. 3-(c)). Beyond this point, as  $K_I$  increases further ( $K_I \gg K_{Ic}$ ), the crack propagates in a certain direction, typically along the

crack plane (*Nr.1*: Fig. 3-(a); *Nr.3*: Fig. 3-(c); *Nr.4*: Fig. 3-(d)). The crack propagation, however, may be more complicated, e.g., following a zigzag pattern (*Nr.2*: Fig. 3-(b); *Nr.5*: Fig. 3-(e)), or growing diagonally across the lattice

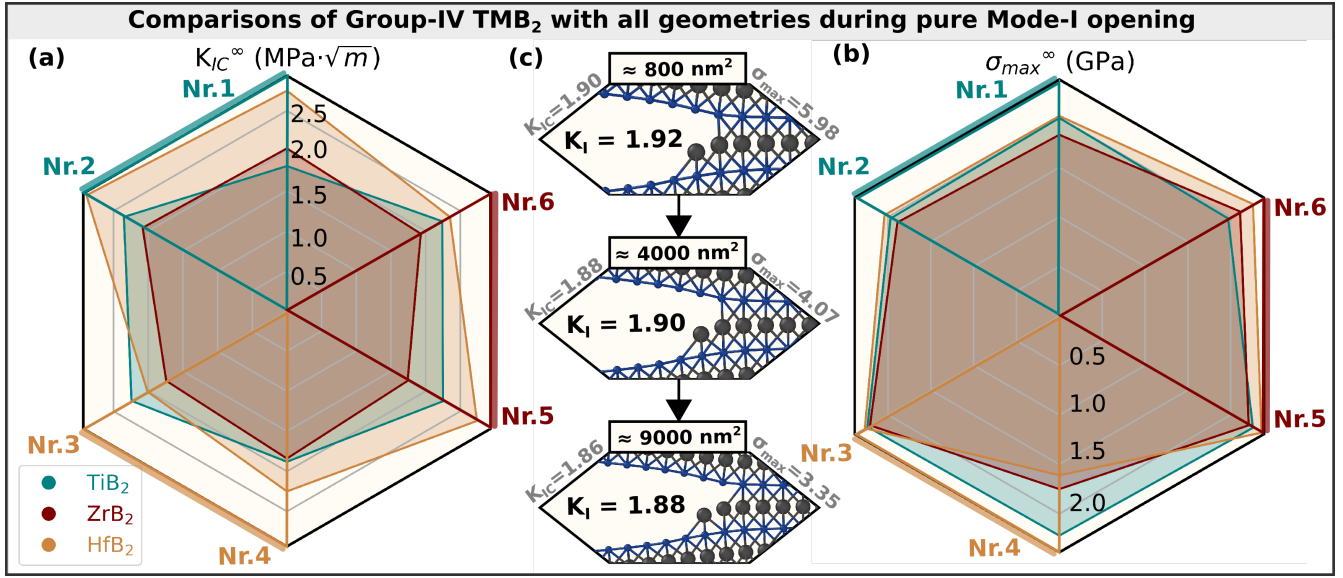


**Figure 4.** Comparison of converged fracture toughness values (a,  $K_{Ic}^{\infty}$ ) and maximum strength (b,  $\sigma_{max}^{\infty}$ ) during Mode-I loading among different TMB<sub>2</sub> compounds and geometries. TiB<sub>2</sub> is shown in teal, ZrB<sub>2</sub> in red, and HfB<sub>2</sub> in orange. The results are ordered counterclockwise from Nr.1 to Nr.6, as defined in Fig. 2. (c) Example of Nr.1 ((0001)[10 $\bar{1}$ 0]) geometry of TiB<sub>2</sub>, with increasing plane area from 800 nm<sup>2</sup> (top) to 9000 nm<sup>2</sup> (down). The zoomed-in screenshot shows the behavior immediately after reaching  $K_{Ic}$ , with the fracture phenomenon remaining similar.

(Nr.6.: Fig. 3-(f)). The detailed mechanisms underlying these propagation behaviors will be analyzed below.

Fig. 4 compares  $K_{Ic}^{\infty}$  (Fig. 4-(a)) and  $\sigma_{max}^{\infty}$  (Fig. 4-(b)) for the Group-IV TMB<sub>2</sub>s, derived as extrapolative values for an infinite plate area. Following Ref.<sup>53</sup>, the data is fitted using a combined inverse polynomial function against the plate area ( $L^2$ )<sup>52</sup>, as further detailed in the supplementary material. Overall, HfB<sub>2</sub> exhibits the highest  $K_{Ic}^{\infty}$  (mainly  $\approx 2.8 \text{ MPa}\cdot\sqrt{m}$ ), except for Nr.3 (TiB<sub>2</sub> is the highest with  $2.24 \text{ MPa}\cdot\sqrt{m}$ , whereas HfB<sub>2</sub> has  $2.01 \text{ MPa}\cdot\sqrt{m}$ ), while ZrB<sub>2</sub> shows the lowest (mainly  $\approx 1.8 \text{ MPa}\cdot\sqrt{m}$ ), except for Nr.1 (TiB<sub>2</sub> is the lowest with  $1.81 \text{ MPa}\cdot\sqrt{m}$ , whereas ZrB<sub>2</sub> has  $2.03 \text{ MPa}\cdot\sqrt{m}$ ). In terms of  $\sigma_{max}^{\infty}$ , the three materials display similar values (mainly  $\approx 2.0 \text{ GPa}$ ), with the notable exception of Nr.4, where TiB<sub>2</sub> demonstrates significantly higher values (TiB<sub>2</sub> remains  $\approx 2.0 \text{ GPa}$ , where the others have  $\approx 1.7 \text{ GPa}$ ). Contrarily to strongly size-dependent fracture mechanisms and nearly size-independent strength subject to uniaxial tensile tests for single crystals<sup>28</sup>, Mode-I opening simulations reveal significant size effects in both strength and  $K_{Ic}$ . However, the crack growth mechanisms remain very similar for TM=Ti, Zr, Hf (Fig. 4-(c)) and are almost independent of the plate size.

Tab. 2 lists the predicted  $K_{Ic}$ s—precisely, the infinite-plate-extrapolation values,  $K_{Ic}^{\infty}$ —together with the Griffith's  $K_{Ic}^G$  estimates derived from the surface energy and zero-Kelvin elastic constants (Tab. 1). Note that  $K_{Ic}^G$  considers ideal fracture surface parallel to the pre-crack<sup>54</sup>, which does not fully capture the fracture behavior observed in our  $K$ -controlled simulations. Overall, the difference between  $K_{Ic}^{\infty}$  and  $K_{Ic}^G$  falls within the range of 0.5–20%, with the exception of Nr.1 and

Nr.2 for HfB<sub>2</sub>, where  $K_{Ic}^G$  is approximately 30% lower than  $K_{Ic}^{\infty}$ . Additional data is provided in the the supplementary material.

During pure Mode-I opening, Group-IV TMB<sub>2</sub> materials exhibit similar behavior, as illustrated in Fig. 5, with one representative example for each plane (Nr.1: Fig. 5-(a), Nr.3: Fig. 5-(b), Nr.6: in Fig. 5-(c)). For Nr.1–Nr.4, the first TM–B bond breaks upon reaching the  $K_{Ic}$  point (as shown in the sub-patterns in each row and Fig. 3-(a-d)), and the opening continues along the corresponding plane: (0001) for Nr.1 and Nr.2 (zigzag path), and ( $\bar{1}2\bar{1}0$ ) for Nr.3 and Nr.4. Contrarily for the (10 $\bar{1}0$ ) plane, differences arise from the bond-breaking sequence after the initial B–B bond breaks at  $K_{Ic}$  (as shown in the sub-patterns and Fig. 3-e,f). In all Group-IV TMB<sub>2</sub> compounds, the crack tip advances primarily through the continuous breaking of TM–B bonds, as B–B bonds are generally much stronger than TM–B bonds in  $\alpha$ -structured TMB<sub>2</sub> compounds<sup>46</sup>. The difference lies in the propagation patterns: in TiB<sub>2</sub>, the breaking sequence forms a zigzag path but remains along the horizontal direction (Fig. 5-(c-1)), whereas in ZrB<sub>2</sub> and HfB<sub>2</sub>, the crack tip advances diagonally along the ( $\bar{1}101$ ) plane (Fig. 5-(c-2,3)). Importantly, despite the predominant crack opening in TiB<sub>2</sub> occurs along the (10 $\bar{1}0$ ) plane, the actual fracture surface is more complex than that assumed by the Griffith's theory, which would disregard the alternations between mirrored diagonal facets. The observed difference in crack propagation patterns may be attributed to the small differences between (10 $\bar{1}0$ ) and ( $\bar{1}101$ ) surface energies.

The fracture toughness from experiment ranges between 1.8–6.8 MPa√m for TiB<sub>2</sub><sup>55–57</sup>, 2.2–5.0 MPa√m for ZrB<sub>2</sub><sup>40,41,58</sup>, and 2.8–7.2 MPa√m for HfB<sub>2</sub><sup>59,60</sup>. These val-

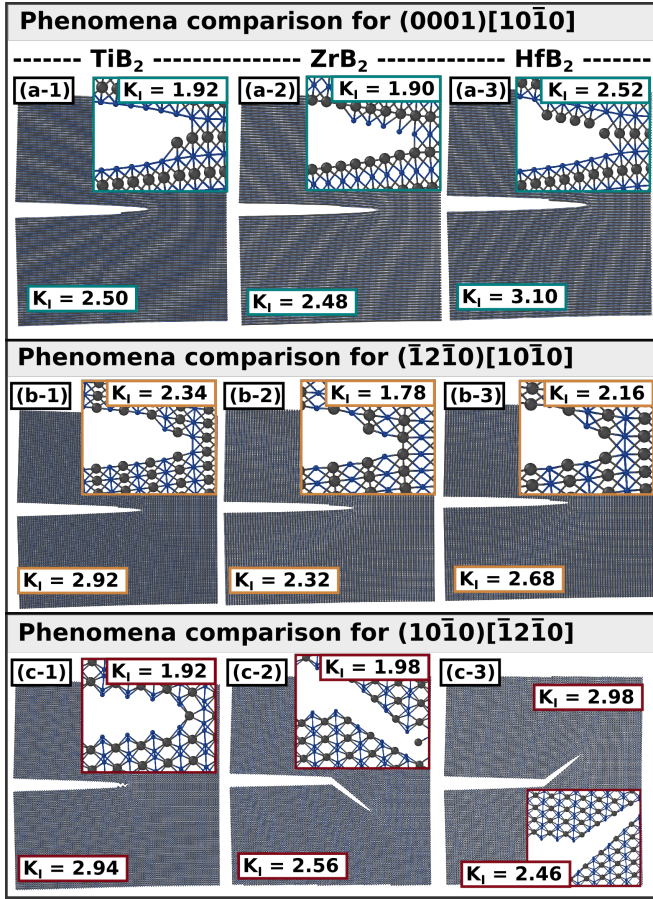


**Figure 5.** Comparison of fracture mechanisms after reaching  $K_{Ic}$  for the studied TMB<sub>2</sub>s, with one example from each crack surface: (a) (0001)[10 $\bar{1}$ 0] (*Nr.1*) for the (0001) plane, (b) ( $\bar{1}$ 2 $\bar{1}$ 0)[10 $\bar{1}$ 0] (*Nr.3*) for the ( $\bar{1}$ 2 $\bar{1}$ 0) plane, and (c) (10 $\bar{1}$ 0)[ $\bar{1}$ 2 $\bar{1}$ 0] (*Nr.6*) for the (10 $\bar{1}$ 0) plane. Mode-I loading results are shown for TiB<sub>2</sub> (\*-1), ZrB<sub>2</sub> (\*-2), and HfB<sub>2</sub> (\*-3). Small, zoomed-in snapshots depict the state shortly after reaching  $K_{Ic}$  ( $K_I = K_{Ic} + 0.02$ , i.e., one step further), while larger, overall snapshots illustrate the fracture behavior well beyond  $K_{Ic}$  ( $K_I > K_{Ic} + 0.50$ ). The dark gray atoms represent metal (TM=Ti, Zr, Hf), as the blue atoms for boron. Plate area of the selected model is  $L^2 \approx 30 \times 30 = 900 \text{ nm}^2$ .

ues align with ML-MS predictions in Fig. 4 and Tab. 2, where the differences between our data and data from various experimental studies (note the significant spread in experimental values) stem from various sample preparation methods, microstructural effects, as well as particular mechanical testing approach. Furthermore, the possibility of mixing with Mode-II shearing or the Mode-III tearing introduces variations in the experimentally obtained  $K_{Ic}$ s. While Mode-III is rather exotic for brittle materials<sup>61</sup>, hence disregarded in this work, mixed Mode-I and Mode-II effects are explored in the following section.

Fig. 5 compares fracture mechanisms of TiB<sub>2</sub>, Zr<sub>2</sub>, and HfB<sub>2</sub> after reaching  $K_{Ic}$ , considering the most experimentally relevant (0001)[10 $\bar{1}$ 0] (*Nr.1*), ( $\bar{1}$ 2 $\bar{1}$ 0)[10 $\bar{1}$ 0] (*Nr.3*), and (10 $\bar{1}$ 0)[ $\bar{1}$ 2 $\bar{1}$ 0] (*Nr.6*) crack geometries. Among them, only the opening in the *Nr.3* geometry (Fig. 5-(b)) shows that each TMB<sub>2</sub> compound breaks the same number of bonds. For the

other two geometries, *Nr.1* (Fig. 5-(a)) and *Nr.6* (Fig. 5-(c)), TiB<sub>2</sub> consistently breaks a single bond, while ZrB<sub>2</sub> and HfB<sub>2</sub> rupture multiple bonds simultaneously. This suggests that stress in ZrB<sub>2</sub> and HfB<sub>2</sub> redistributes more effectively, leading to abrupt fracture. Despite their high  $G/B$  values among all TMB<sub>2</sub>s—indicating intrinsic brittleness<sup>46,62</sup>—variations in crack-tip shielding, bond anisotropy, or localized deformation mechanisms further influence the fracture behavior.

#### 4 Mixed Mode-I and Mode-II loading: example of TiB<sub>2</sub>

Due to the material's heterogeneity, the sample's geometry, or loading conditions, achieving a pure Mode-I fracture in experiments is rare<sup>63–65</sup>. Even a slight misalignment in combination with microstructural effects (e.g., grain boundaries, phase interfaces) can introduce shear components, leading to mixed-mode fracture<sup>66–68</sup>. In this section, we focus on mixed Mode-I and Mode-II crack opening, using TiB<sub>2</sub> together with the ( $\bar{1}$ 2 $\bar{1}$ 0)[10 $\bar{1}$ 0] (*Nr.3*), and (10 $\bar{1}$ 0)[ $\bar{1}$ 2 $\bar{1}$ 0] (*Nr.6*) crack geometries as an example.

Fig. 6 illustrates effects of the Mode-I fraction on the nucleation of cracks parallel to ( $\bar{1}$ 2 $\bar{1}$ 0) plane with [10 $\bar{1}$ 0] front direction (( $\bar{1}$ 2 $\bar{1}$ 0)[10 $\bar{1}$ 0]). There is a gradual increase in  $K_{Ic}$  with a higher Mode-I fraction (Fig. 6-a), rising from  $K_{Ic} = 1.92 \text{ MPa}\sqrt{m}$  for pure Mode-II to  $K_{Ic} = 2.23 \text{ MPa}\sqrt{m}$  for pure Mode-I. However, within the range of 0% to 20% Mode-I fraction, a slight decrease is observed, with  $K_c^{Mix}$  dropping from 1.92 to 1.84  $\text{MPa}\sqrt{m}$ . Fig. 6-(b) presents a distance map corresponding to the deformation stage when the step reaches 50–85% of  $K_c$ , highlighting the distance from the crack tip to the border and showing the stress distribution during deformation. A distinct fracture mechanisms corresponding to Mode-I and Mode-II loading are observed. Fig. 6-(c,d) depicts four distinct crack propagation mechanisms that occur during ( $\bar{1}$ 2 $\bar{1}$ 0)[10 $\bar{1}$ 0] deformation.

Starting with pure Mode-I opening, the crack propagates predominantly along the ( $\bar{1}$ 2 $\bar{1}$ 0) plane. As the Mode-I fraction decreases to 70%, the crack propagation shifts entirely to the ( $\bar{1}$ 2 $\bar{1}$ 0) plane, indicating a transition in the crack path and initiating a pyramidal slip. This behavior is consistent with observations of both tensile<sup>28</sup> and shear<sup>29</sup> deformation in TiB<sub>2</sub>, aligning with the studied preferred failure plane. At 60% Mode-I fraction, the crack first propagates along the (0001) plane before transitioning to the ( $\bar{1}$ 2 $\bar{1}$ 0) plane. Below 50% Mode-I fraction, and continuing to the pure Mode-II case, the structure opens along the (0001) plane once  $K_c$  is reached. This is similar to crack growth mechanism observed in the ( $\bar{1}$ 2 $\bar{1}$ 0)[0001] (*Nr.4*) loading geometry. For further details, refer to the supplementary material.

The (10 $\bar{1}$ 0)[ $\bar{1}$ 2 $\bar{1}$ 0] (*Nr.6*) deformation (Fig. 7-(a)) shows more intricate  $K_c^{Mix}$  trends, with a local minimum,  $K_c^{Mix} = 1.32 \text{ MPa}\sqrt{m}$ , around 60% of Mode-I. The values for pure Mode-I and pure Mode-II are fairly similar, with  $K_{Ic} = 1.72 \text{ MPa}\sqrt{m}$  and  $K_{Ic} = 1.94 \text{ MPa}\sqrt{m}$ , respectively. Fig. 7-(b), featuring a distance map, illustrates the distance from the

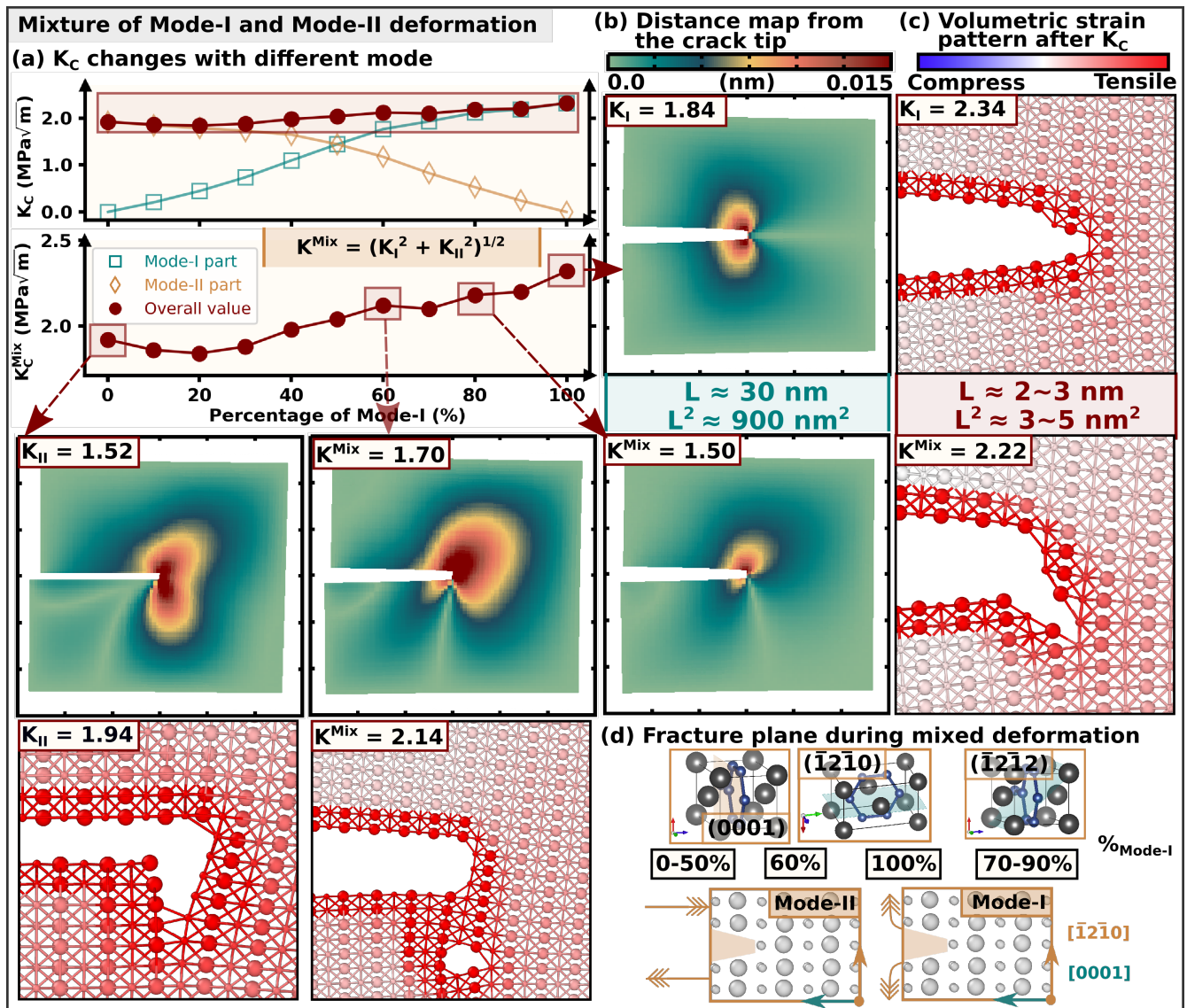


**Figure 6. Mixed Mode-I and Mode-II loading exemplified by  $TiB_2$  and the  $(\bar{1}2\bar{1}0)[10\bar{1}0]$  ( $Nr:3$ ) crack geometry.** (a)  $K_c$  point showing separate Mode-I (teal), Mode-II (orange), and Mode-Mix (red), with an additional zoomed-in curve for the Mode-Mix. (b) Distance map from the crack tip for  $K_c \cdot 0.5 < K < K_c \cdot 0.8$  for selected ratios. (c) Volumetric strain pattern with a magnification of the crack tip region for  $K = K_c + 0.02$ , with a reference configuration being the pre-cracked structure at  $K = 0$  (not the defect-free ideal structure). The selected ratios are: 0% (pure Mode-II), 60%, 80% and 100% (pure Mode-I), corresponding to the transition of the fracture plane shown in (d), demonstrating four different mechanisms and three distinct fracture planes with varying ratios.

crack tip and highlights the differences in stress contributions between Mode-I and Mode-II deformation. Combined with Fig. 7-(c) and (d), this deformation exhibits distinct behavior across varying Mode-I contributions. In pure Mode-I loading, the crack propagates in a zigzag pattern by opening along mirrored diagonal facets while maintaining an overall horizontal direction. From 90% down to 60% Mode-I fractions, the material opens along the  $(\bar{1}\bar{1}01)$  plane after reaching  $K_c$ , aligning with the first pyramidal slip plane and the preferred pure Mode-I opening plane for  $ZrB_2$  and  $HfB_2$  (Fig. 5-(c)). Interestingly, between 50% and 10% Mode-I, the  $TiB_2$  initially slips along the basal plane, then opens along the same

plane. A similar slip behavior is also observed during the  $(0001)[\bar{1}2\bar{1}0]$  shear deformation in other  $TMB_2$  compounds,  $TM=Ta, W, Re$ <sup>29</sup>. Between 10% Mode-I and pure Mode-II, the structure transitions to opening exclusively along the  $(0001)$  plane without any prior slipping. The transition from Mode-I to Mode-II in  $Nr:5$  deformation ( $(10\bar{1}0)[0001]$ ) follows an expectable pattern. The crack propagates through the  $(10\bar{1}0)$  plane from pure Mode-I to 90% Mode-I, but in a flat manner rather than a zigzag pattern. Between 80% and 70% Mode-I, the crack shifts to the  $(11\bar{2}0)$  plane, and for all percentages below this, down to pure Mode-II, it propagates through the  $(\bar{1}\bar{1}00)$  plane. These transitions indicate prismatic

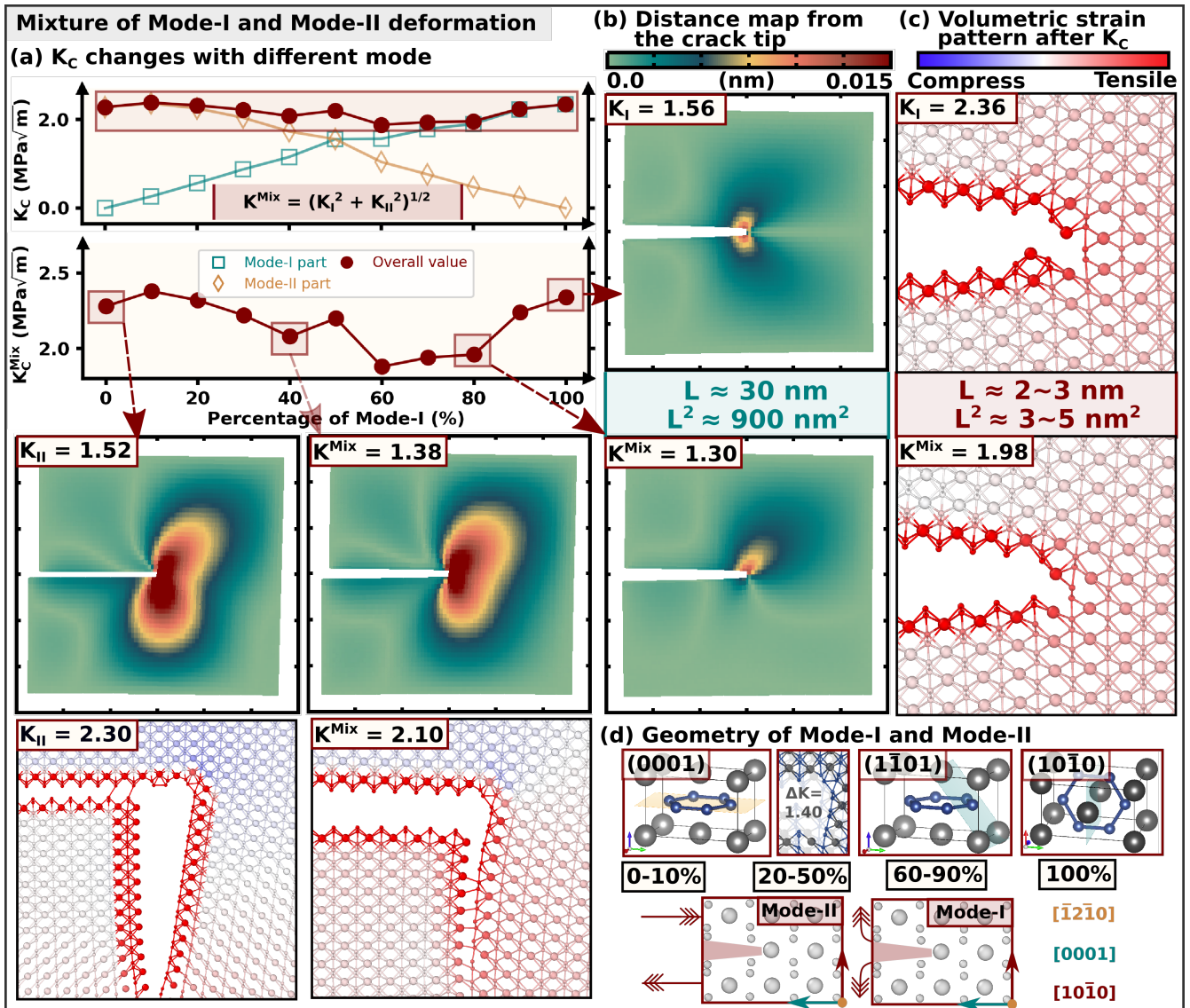


**Figure 7. Mixed Mode-I and Mode-II loading exemplified by  $TiB_2$  and the  $(10\bar{1}0)[\bar{1}2\bar{1}0]$  ( $Nr:6$ ) crack geometry.** (a)  $K_c$  point showing separate Mode-I (teal), Mode-II (orange), and Mode-Mix (red), with an additional magnification of the Mode-Mix. (b) Distance map from the crack tip when  $K_c \cdot 0.5 < K < K_c \cdot 0.8$  for selected ratios. (c) Volumetric strain pattern with a magnification of the crack tip region for  $K = K_c + 0.02$ , with a reference configuration being the pre-cracked structure at  $K = 0$  (not the defect-free ideal structure). The selected ratios are: 0% (pure Mode-II), 40%, 80% and 100% (pure Mode-I), corresponding to the transition of the fracture plane shown in (d), demonstrating four different mechanisms and three distinct fracture planes with varying ratios.

slip occurring after reaching  $K_c$ . For additional details, refer to the Supplementary material.

Furthermore, the fracture toughness results for the  $(\bar{1}2\bar{1}0)[10\bar{1}0]$  and  $(10\bar{1}0)[\bar{1}2\bar{1}0]$  geometries exhibit minimal differences (of similar magnitude) between  $K_{Ic}$  and  $K_{IIc}$ , indicating that the resistance of  $TiB_2$  to crack propagation remains consistent in these two perpendicular planes ( $(\bar{1}2\bar{1}0)$  and  $(10\bar{1}0)$ ). Since these configurations share a common normal direction along the  $[0001]$ -axis, this underlines the basal plane isotropy of  $TiB_2$ , previously shown for elastic constants, tensile and shear strengths<sup>28,29</sup>.

## 5 Experimental testing and verification of model

To support results of atomistic simulations, we conduct cube-corner nanoindentation tests on  $TiB_2$  thin films with near 1:2 Ti-to-B stoichiometry. The film's structure prior to as well as after nanoindentation is observed using high-resolution transmission electron microscopy (HRTEM). As typical for  $TiB_2$ 's, our as-deposited  $TiB_2$  films are  $[0001]$ -oriented (Fig. 8-(a)). Following post-mortem HRTEM analysis (Fig. 8-(b)), a similarity between experiment and ML-MS simulations of  $(10\bar{1}0)[\bar{1}2\bar{1}0]$  loading ( $Nr:6$ ) crack geometry is deduced.

As cube-corner indentation tests generally induce mixed



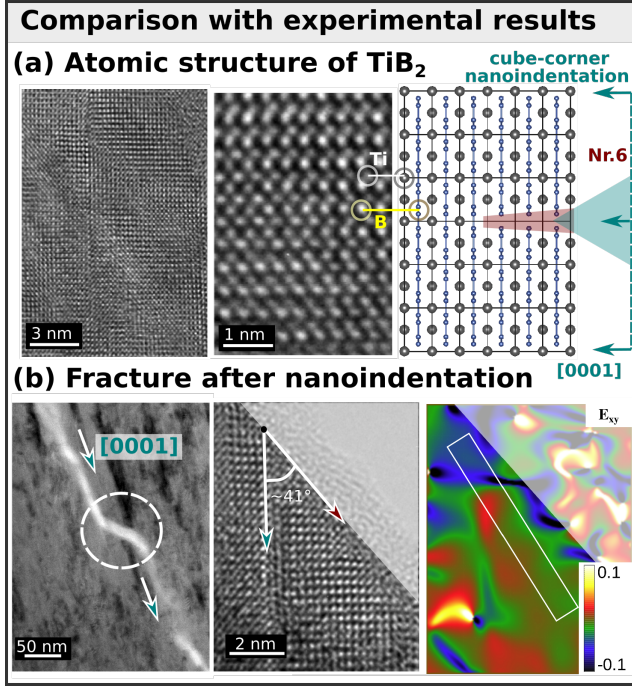


**Figure 8.** Comparison of simulation and experimental results for TiB<sub>2</sub>. (a) Atomic structure of TiB<sub>2</sub> thin film from HRTEM prior to nanoindentation, compared with the atomistic model used for pre-crack simulations, with the [0001] direction indicated. The brighter pattern represents two B atoms merging together, while the relatively darker pattern corresponds to Ti atoms. (b) HRTEM pattern after cube-corner nanoindentation, showing angle changes during fracture. The average shear strain,  $E_{xy}$ , is highlighted using the geometric phase analysis (GPA) pattern.

Mode-I (dominant) and Mode-II opening<sup>69</sup>, we use the Mixed-Mode simulations to find correlations with HRTEM observations. Specifically, a crack growth under  $\approx 40^\circ$  is shown in Fig. 8-(b). This can be mimicked by simulations with  $< 40\%$  Mode-II fraction, during which crack propagates along the  $(1\bar{1}01)$  plane, consistently with low energetic costs of prismatic and pyramidal slip in AIB<sub>2</sub>-type materials<sup>70,71</sup>. The strain distribution map (obtained from TEM using the geometric phase analysis, GPA) indicates an average shear strain of  $\approx 5\%$  near the crack region, underscoring the presence of Mode-II deformation. The fracture toughness of our TiB<sub>2</sub> sample is measured as  $3.08 \text{ MPa}\sqrt{m}$ <sup>45</sup>, which is approximately 40% higher than both our simulated value ( $K_{Ic}^\infty$ ) and the theoretical value predicted by Griffith's theory ( $K_{Ic}^G$ ). The experimental  $K_{Ic}$ , however, represents the fracture toughness across the entire sample, which has a slightly boron-rich composition (TiB<sub>2.04</sub>). The boron-rich tissue phase likely reduces fracture toughness, while TiB<sub>4.42</sub> exhibits a  $K_{Ic}$  of  $2.51 \text{ MPa}\sqrt{m}$ <sup>45</sup>.

Although the idealized Griffith assumption does not fully capture the fracture behavior observed in our  $K$ -controlled simulations (under pure Mode-I) and experiments (a mixture of Mode-I and Mode-II), it remains a useful reference. Griffith's theory is based on purely elastic behavior, neglecting inelastic deformation. In contrast, our  $K$ -controlled simulations incorporate atomic-scale effects such as plasticity and bond-

breaking mechanisms, all of which influence crack propagation and lead to deviations from the purely elastic prediction. Additionally, while the  $K$ -controlled approach assumes linear elastic fracture mechanics (LEFM)<sup>53,72</sup>, atomic-scale phenomena introduce nonlinear effects, including bond stretching and local stress concentrations in interatomic potentials. These factors collectively contribute to the observed differences between the fracture toughness values obtained from Griffith's theory and those from our simulations. While modifications by McClintock and Walsh<sup>73</sup> account for plastic effects, the Griffith approach remains a relatively objective method for evaluating the fracture toughness of brittle materials.

## 6 Conclusion

To investigate inherent fracture properties of the Group-IV transition metal diborides, TMB<sub>2</sub>:s (TM=Ti, Zr, Hf),  $K$ -controlled molecular statics simulations were performed using pre-cracked models and own machine-learning interatomic potentials. We demonstrated the suitability of MLIPs for determining the fracture toughness and fracture strength of hard but brittle solids, thus pointing to a route for systematically classifying the fracture properties of materials.

The validation against DFT and finite-temperature *ab initio* MD calculations confirmed the reliability of here-trained MLIPs, with tensile strength, elastic constants, and surface energy showing sufficient accuracy. Our main focus was on the pure Mode-I fracture (representing ideal brittle failure), considering six low-index crack geometries:  $(0001)[10\bar{1}0]$  (*Nr.1*),  $(0001)[\bar{1}2\bar{1}0]$  (*Nr.2*),  $(\bar{1}2\bar{1}0)[10\bar{1}0]$  (*Nr.3*),  $(\bar{1}2\bar{1}0)[0001]$  (*Nr.4*),  $(10\bar{1}0)[0001]$  (*Nr.5*),  $(10\bar{1}0)[\bar{1}2\bar{1}0]$  (*Nr.6*). While the maximum strength remained similar ( $\approx 2.0 \text{ GPa}$ ) for the studied TMB<sub>2</sub>:s (except for one crack geometry), fracture toughness ordered as:  $\text{HfB}_2 (\approx 2.7 \text{ MPa}\sqrt{m}) > \text{TiB}_2 (\approx 2.3 \text{ MPa}\sqrt{m}) > \text{ZrB}_2 (\approx 1.8 \text{ MPa}\sqrt{m})$ , with minor deviations in two geometries. Additionally, although most results aligned well with Griffith's predictions, discrepancies arose due to crack propagation not always confined to the ideal crack plane but sometimes diverted in a diagonal or zigzag-like manner.

With the example of TiB<sub>2</sub> and the  $(\bar{1}2\bar{1}0)[10\bar{1}0]$  and  $(10\bar{1}0)[\bar{1}2\bar{1}0]$  crack geometries (motivated by typical [0001] orientation of TMB<sub>2</sub> thin films), effects of mixed Mode-I and Mode-II deformation on fracture toughness and mechanisms were investigated. Our simulations revealed that even a small Mode-II component can significantly alter fracture behavior. Furthermore, we conducted cube-corner nanoindentation tests, typically considered a pure Mode-I loading. The local strain distribution—mapped using the geometric phase analysis (GPA)—indicated a  $\approx 5\%$  shear strain component, pointing towards the contribution of Mode-II deformation. The observed sample orientation in the as deposited state and the nanoindentation-induced crack growth was correlated with our ML-MS simulations of mixed Mode-I and II loading, with the Mode-II component below 40%.

Our work shows that  $K$ -controlled simulations can provide

an atomistic view of nanoscale mechanical response to crack growth, yielding reliable  $K_c$  values while incorporating plasticity and bond-breaking effects that influence propagation and cause deviations from purely elastic predictions. While finite-temperature effects have not been explicitly considered, the strong agreement between *ab initio*MD and ML-MD simulations suggests the potential for extending the pre-crack model to more complex environmental conditions. Overall, the presented simulation approach can serve a powerful tool for analyzing fracture toughness and behavior in complex ceramics, paving the path towards systematic predictions of fracture-related descriptors and mechanisms.

## Methods

### Ab initio calculations

Finite-temperature Born-Oppenheimer *ab initio* molecular dynamics (*ab initio* MD) calculations were carried out using VASP<sup>74</sup> together with the projector augmented wave (PAW)<sup>75</sup> method and the Perdew-Burke-Ernzerhof exchange-correlation functional revised for solids (PBEsol)<sup>76</sup>. The plane-wave cut-off energies of 300 eV and  $\Gamma$ -point sampling of the reciprocal space were employed.

**Structural models** of TMB<sub>2</sub>s, TM=(Ti, Zr, Hf) were based on the  $\alpha$  polymorph, adopting A1B<sub>2</sub>-type (P6/mmm) phase<sup>51,77</sup>. The hexagonal unit cells were orthogonalized using the following crystallographic orientations:  $x \parallel [10\bar{1}0]$ ,  $y \parallel [\bar{1}2\bar{1}0]$ ,  $z \parallel [0001]$ . All *ab initio* MD calculations were conducted using 720-atom supercells (240 TM+480 B) with dimensions of  $\approx (1.5 \times 1.6 \times 2.6)$  nm<sup>3</sup>. The supercells were equilibrated at target temperature (300 K and 1200 K) through a two-step process: (i) a 10 ps isobaric-isothermal (NpT) simulation using a Parrinello-Rahman barostat<sup>78</sup> and Langevin thermostat; (ii) a 2–4 ps simulation with the canonical (NVT) ensemble based on Nosé-Hoover thermostat, applying the time-averaged lattice parameters obtained from (i).

**Room-temperature elastic constants**,  $C_{ij}$ , were determined following Ref.<sup>79</sup>, i.e., obtained from a second-order polynomial fit of stress/strain data from the [0001], [10 $\bar{1}0$ ], and [ $\bar{1}2\bar{1}0$ ] tensile simulations (used to derive  $C_{11}$ ,  $C_{12}$ ,  $C_{13}$ ,  $C_{33}$ ), and the (0001)[ $\bar{1}2\bar{1}0$ ], (10 $\bar{1}0$ )[ $\bar{1}2\bar{1}0$ ] and (10 $\bar{1}0$ )[0001] shear simulations (used to derive  $C_{44}$ ). Strains ranging from 0 to 4% were considered. Stress tensor components were calculated by averaging data over the last 0.5 ps of each simulation.

**Zero Kelvin elastic constants** were also calculated using the stress-strain method, with the same energy convergence criteria as the *ab initio* MD calculations but smaller strain (up to 1%). The methodology is consistent with our previous work<sup>28</sup>, concerning  $C_{ij}$  of  $\alpha$ -TiB<sub>2</sub>. The **surface energies** were calculated at zero Kelvin using a 60-atom TiB<sub>2</sub> supercell (with a  $3 \times 3 \times 1$  k-mesh and cut-off energy of 300 eV) together with a 12 Å vacuum layer.

### Molecular statics/dynamics with MLIPs (ML-MS/MD)

ML-MS calculations were conducted using the LAMMPS code<sup>80</sup> interfaced with the mlip-2 package<sup>27</sup> enabling the

usage of MTP-type MLIPs. Active learning has been performed using the concept of extrapolation grade, MV<sup>81</sup>, which also served to assess the reliability during MD simulations with the trained MLIPs. For MLIP **validation** purposes, we performed MD simulations of uniaxial deformation and calculated elastic constants. Computational setup for equilibration and tensile tests at the atomic scale was designed to closely match the corresponding *ab initio* MD simulations. For zero-Kelvin elastic constant validation, to minimize variables and maintain accuracy, we conducted MD calculations at 10 K instead of using MS simulations. A detailed discussion of MD validation is provided in the supplementary material. The zero-Kelvin surface energies were validated using ML-MS with 12 Å vacuum, the same as in DFT calculations.

**K-controlled MS simulations** were utilized to evaluate the effective resistance to brittle cleavage, using cracked-plate models of sizes reaching  $\approx 10^6$  atoms ( $L^2 \approx 250^2$  nm<sup>2</sup>, where  $L$  is the lateral size). Theory and methods followed Refs.<sup>53,72,82</sup>. We employed square TMB<sub>2</sub> plates (with area of  $L^2$ ) with all the possible geometries for both Mode-I and Mode-II loadings, i.e., (0001)[10 $\bar{1}0$ ] (*Nr.1*), (0001)[ $\bar{1}2\bar{1}0$ ] (*Nr.2*), ( $\bar{1}2\bar{1}0$ )[10 $\bar{1}0$ ] (*Nr.3*), ( $\bar{1}2\bar{1}0$ )[0001] (*Nr.4*), (10 $\bar{1}0$ )[0001] (*Nr.5*), (10 $\bar{1}0$ )[ $\bar{1}2\bar{1}0$ ] (*Nr.6*). The supercells were periodic along the crack-front direction with the thickness of approximately 0.5 nm. Atoms in the frame region centered at the crack tip are sequentially displaced by incrementing the crack-tip stress intensity  $K_I$ ,  $K_{II}$ , and  $K_{mix}$  at steps of 0.02 MPa $\sqrt{m}$ , while during Mode-Mix the  $K$ s are calculated as follows:  $K_{mix} = \sqrt{K_I^2 + K_{II}^2}$ ,  $K_I = K_{mix} \cdot \frac{a}{\sqrt{a^2+b^2}}$ ,  $K_{II} = K_{mix} \cdot \frac{b}{\sqrt{a^2+b^2}}$  (percentage), where  $a$  is the content of Mode-I,  $b$  for Mode-II, and  $a + b = 100$ . All, except frame atoms, were relaxed with the conjugate-gradient algorithm at each  $K$  increment, with the tolerances are set to  $10^{-14}$  for energy changes and  $10^{-14}$  eV/Å for forces. The simulations were carried out with atomically sharp cracks, where interactions between atoms on opposite sides of the crack plane were screened over  $\approx 1$  nm. Further, half rows of atoms were deleted, and the plates are constructed with an equal number of atomic layers above and below the crack.

The **Griffith fracture toughness**,  $K_{Ic}^G$ , was derived from<sup>83</sup>:

$$K_{Ic}^G = [2E_{sur}^{un} f \Lambda_{22}^{-1}]^{1/2} \quad (1)$$

where  $E_{sur}^{un}$  represents the unrelaxed surface energy and  $\Lambda_{22}^{-1}$  is an element from the inverse of the Stroh energy tensor ( $\bar{\bar{\Lambda}}$ ), calculated from the elastic tensor.

### Experimental methods

A TiB<sub>2.04</sub> coating with near 1:2 stoichiometry and approximately 2  $\mu$ m thickness was provided for analysis. The coating was deposited using an in-house DC balanced magnetron sputtering system, employing a 6-inch, powder-metallurgically produced TiB<sub>2</sub>/C (99/1 wt.%) target (>99.6% purity). The

complete deposition procedure is detailed in Ref.<sup>45</sup>. Nanoindentation tests were performed using an FT-I04 Femto-Indenter equipped with a cube-corner diamond tip to induce controlled cracking. A total of 17 indents were applied at peak loads ( $F_m$ ) ranging from 50 to 450 mN. The tests followed a displacement-controlled loading-unloading cycle. A cross-sectional TEM lamella was extracted from a radial crack tip using a Thermo Scientific Scios 2 DualBeam FIB-SEM system. Following a conventional FIB milling and lift-out procedure as presented in Ref.<sup>84</sup>, an 8  $\mu\text{m}$  thick tungsten protection layer was deposited over the region of interest to prevent milling damage. Initially, a 2  $\mu\text{m}$  thick cross-sectional lamella was prepared, which was then refined by sequential ion milling steps to approximately 100 nm. Final cleaning steps at 2 kV and 27 pA, followed by Ar ion milling at 0.5 kV using a Gatan PIPS II system, further reduced the thickness to <75 nm, allowing high-resolution TEM analysis.

The cross-sectional transmission electron microscopy (TEM) specimens were prepared using an FEI Quanta 200 3D DBFIB. A 200 kV field emission TEM (JEOL 2100F) equipped with an image-side spherical aberration ( $C_s$ )-corrector was used in the high-resolution TEM (HRTEM) study, demonstrating a resolution of 1.2 Å at 200 kV. The aberration coefficient was set close to zero, under which the HRTEM images were taken under slightly over-focus conditions (close to the Scherzer defocus). A CCD Orius camera is used to record HRTEM images, where image sizes are 2048 pixels  $\times$  1336 pixels. The strain fields in  $\text{TiB}_2$  were calculated based on the  $C_s$ -corrected HRTEM images by the geometric phase analysis (GPA) method. According to the GPA algorithm, the displacement fields can be obtained by selecting two non-collinear Bragg vectors in the power spectrum generated from a high-resolution TEM image.

## Acknowledgements

LH acknowledges financial support from the Swedish Government Strategic Research Area in Materials Science on Functional Materials at Linköping University SFO-Mat-LiU No. 2009 00971. Support from Knut and Alice Wallenberg Foundation Scholar Grants KAW2016.0358 and KAW2019.0290 is also acknowledged by LH. DGS gratefully acknowledges financial support from the Swedish Research Council (VR) through Grant N° VR-2021-04426 and the Competence Center Functional Nanoscale Materials (FunMat-II) (Vinnova Grant No. 2022-03071). The financial support (Z.C. and Z.Z.) by the Austrian Science Fund (FWF P33696) is highly acknowledged. The authors acknowledge original  $\text{TiB}_2$  samples from Anna Viktoria Hirle, also for providing the raw data from previous publication<sup>45</sup> and participating discussion. PHM and NK acknowledge the Austrian Science Fund, FWF (10.55776/PAT4425523). The FFG projects: Bridge and iDAP+ are further acknowledged by PHM. We sincerely thank the Electron Microscopy Center at USTEM TU Wien for FIB-SEM access. The computations handling were enabled by resources provided by the National Academic In-

frastructure for Supercomputing in Sweden (NAISS) and the Swedish National Infrastructure for Computing (SNIC) at the national supercomputer center (NSC) partially funded by the Swedish Research Council through grant agreements no. 2022-06725 and no. 2018-05973, as well as by the Vienna Scientific Cluster (VSC) in Austria. The authors acknowledge TU Wien Bibliothek for financial support through its Open Access Funding Program.

## CRedit author contributions statement

**SL:** Methodology, Investigation, Data curation, Formal analysis, Visualization, Writing - original draft. **ZC:** Investigation, Writing - review & editing **RJ:** Investigation, Writing - review & editing **ZZ, LH, PHM:** Resources, Funding acquisition, Writing - review & editing **NK:** Conceptualization, Methodology, Supervision, Writing - review & editing **DGS:** Conceptualization, Methodology, Software, Investigation, Writing - review & editing

## Conflicts of interest

The authors declare that they have no known competing financial interests or personal relationships that could have appeared to influence the work reported in this paper.

## Data availability

Data will be made available on request.

## References

1. A. A. Griffith, "On the phenomena of rupture and flow in solids," *Proc R Soc Lond A Math Phys Sci*, vol. 221, no. 582-593, pp. 163–198, 1921.
2. G. R. Irwin, "Analysis of stresses and strains near the end of a crack traversing a plate," *American Society of Mechanical Engineers*, 1957.
3. T. Nose and T. FUJII, "Evaluation of fracture toughness for ceramic materials by a single-edge-precracked-beam method," *J. Am. Ceram. Soc.*, vol. 71, no. 5, pp. 328–333, 1988.
4. T. L. Anderson, M. Dawes, and H. McHenry, *Elastic-plastic fracture toughness tests with single-edge notched bend specimens*. ASTM International, 1985.
5. E. M. Shaji, S. R. Kalidindi, R. D. Doherty, and A. S. Sedmak, "Plane strain fracture toughness of MP35N in aged and unaged conditions measured using modified CT specimens," *Mater. Sci. Eng. A*, vol. 340, no. 1-2, pp. 163–169, 2003.
6. J. Underwood, S. Freiman, F. Baratta, *et al.*, "A review of chevron-notched fracture specimens," in *Chevron-notched Specimens, Testing and Stress Analysis: A Symposium*, vol. 855, p. 5, ASTM International, 1984.

7. R. Kolhe, C.-Y. Hui, and A. T. Zehnder, "Effects of finite notch width on the fracture of chevron-notched specimens," *Int. J. Fract.*, vol. 94, pp. 189–198, 1998.
8. B. Gludovatz, S. Wurster, A. Hoffmann, and R. Pippan, "Fracture toughness of polycrystalline tungsten alloys," *Int. J. Refract. Met. Hard Mater.*, vol. 28, no. 6, pp. 674–678, 2010.
9. M. E. Launey and R. O. Ritchie, "On the fracture toughness of advanced materials," *Adv. Mater.*, vol. 21, no. 20, pp. 2103–2110, 2009.
10. X. Zeng and A. Hartmaier, "Modeling size effects on fracture toughness by dislocation dynamics," *Acta Mater.*, vol. 58, no. 1, pp. 301–310, 2010.
11. J. J. Möller and E. Bitzek, "Fracture toughness and bond trapping of grain boundary cracks," *Acta Mater.*, vol. 73, pp. 1–11, 2014.
12. T. Shimokawa, M. Tanaka, K. Kinoshita, and K. Higashida, "Roles of grain boundaries in improving fracture toughness of ultrafine-grained metals," *Phys. Rev. B Condens. Matter*, vol. 83, no. 21, p. 214113, 2011.
13. S. Samborski and T. Sadowski, "Dynamic fracture toughness of porous ceramics," *J. Am. Ceram. Soc.*, vol. 93, no. 11, pp. 3607–3609, 2010.
14. H.-J. Kleebe, G. Pezzotti, and G. Ziegler, "Microstructure and fracture toughness of Si<sub>3</sub>N<sub>4</sub> ceramics: combined roles of grain morphology and secondary phase chemistry," *J. Am. Ceram. Soc.*, vol. 82, no. 7, pp. 1857–1867, 1999.
15. Z. Zhang, A. Ghasemi, N. Koutná, Z. Xu, T. Grünstäudl, K. Song, D. Holec, Y. He, P. H. Mayrhofer, and M. Bartosik, "Correlating point defects with mechanical properties in nanocrystalline TiN thin films," *Mater. Des.*, vol. 207, p. 109844, 2021.
16. L. Ma, A.-L. Fauchille, M. R. Chandler, P. Dowey, K. G. Taylor, J. Mecklenburgh, and P. D. Lee, "In-situ synchrotron characterisation of fracture initiation and propagation in shales during indentation," *Energy*, vol. 215, p. 119161, 2021.
17. K. Fadenberger, I. E. Gunduz, C. Tsotsos, M. Kokonou, S. Gravani, S. Brandstetter, A. Bergamaschi, B. Schmitt, P. H. Mayrhofer, C. C. Doumanidis, *et al.*, "In situ observation of rapid reactions in nanoscale Ni–Al multilayer foils using synchrotron radiation," *Appl. Phys. Lett.*, vol. 97, no. 14, 2010.
18. Y. Mishin, "Machine-learning interatomic potentials for materials science," *Acta Mater.*, vol. 214, p. 116980, 2021.
19. D. Dragoni, T. D. Daff, G. Csányi, and N. Marzari, "Achieving DFT accuracy with a machine-learning interatomic potential: Thermomechanics and defects in bcc ferromagnetic iron," *Phys. Rev. Mater.*, vol. 2, no. 1, p. 013808, 2018.
20. T. Mueller, A. Hernandez, and C. Wang, "Machine learning for interatomic potential models," *J. Chem. Phys.*, vol. 152, no. 5, 2020.
21. L. Zhang, G. Csányi, E. van der Giessen, and F. Maresca, "Efficiency, accuracy, and transferability of machine learning potentials: Application to dislocations and cracks in iron," *Acta Mater.*, vol. 270, p. 119788, 2024.
22. J. Behler, "Perspective: Machine learning potentials for atomistic simulations," *J. Chem. Phys.*, vol. 145, no. 17, 2016.
23. V. L. Deringer, M. A. Caro, and G. Csányi, "Machine learning interatomic potentials as emerging tools for materials science," *Adv. Mater.*, vol. 31, no. 46, p. 1902765, 2019.
24. Y. Zuo, C. Chen, X. Li, Z. Deng, Y. Chen, J. Behler, G. Csányi, A. V. Shapeev, A. P. Thompson, M. A. Wood, *et al.*, "Performance and Cost Assessment of Machine Learning Interatomic Potentials," *J. Phys. Chem. A*, vol. 124, no. 4, pp. 731–745, 2020.
25. J. S. Smith, O. Isayev, and A. E. Roitberg, "ANI-1: an extensible neural network potential with DFT accuracy at force field computational cost," *Chem. Sci.*, vol. 8, no. 4, pp. 3192–3203, 2017.
26. A. V. Shapeev, E. V. Podryabinkin, K. Gubaev, F. Tasnádi, and I. A. Abrikosov, "Elinvar effect in  $\beta$ -Ti simulated by on-the-fly trained moment tensor potential," *New J. Phys.*, vol. 22, no. 11, p. 113005, 2020.
27. I. S. Novikov, K. Gubaev, E. V. Podryabinkin, and A. V. Shapeev, "The MLIP package: moment tensor potentials with MPI and active learning," *Mach. learn.: sci. technol.*, vol. 2, no. 2, p. 025002, 2020.
28. S. Lin, L. Casillas-Trujillo, F. Tasnádi, L. Hultman, P. H. Mayrhofer, D. G. Sangiovanni, and N. Koutná, "Machine-learning potentials for nanoscale simulations of tensile deformation and fracture in ceramics," *Npj Comput. Mater.*, vol. 10, no. 1, p. 67, 2024.
29. S. Lin, D. Holec, D. Sangiovanni, T. Leiner, L. Hultman, P. Mayrhofer, and N. Koutná, "Shear-activated phase transformations of diborides via machine-learning potential molecular dynamics," *Preprint*, vol. 10.21203/rs.3.rs-5327540/v1, 2024.
30. N. Koutná, S. Lin, L. Hultman, D. G. Sangiovanni, and P. H. Mayrhofer, "Machine-learning potentials for structurally and chemically complex MAB phases: strain hardening and ripplocation-mediated plasticity," 2025.
31. C. Sevik, J. Bekaert, M. Petrov, and M. V. Milošević, "High-temperature multigap superconductivity in two-dimensional metal borides," *Phys. Rev. Mater.*, vol. 6, no. 2, p. 024803, 2022.
32. H. Holleck, "Material selection for hard coatings," *J. Vac. Sci. Technol.*, vol. 4, no. 6, pp. 2661–2669, 1986.

33. C. Wang, S. Akbar, W. Chen, and V. Patton, "Electrical properties of high-temperature oxides, borides, carbides, and nitrides," *J. Mater. Sci.*, vol. 30, pp. 1627–1641, 1995.
34. H. Waldl, M. Tkadletz, A. Lechner, C. Czettel, M. Pohler, and N. Schalk, "Evolution of the fracture properties of arc evaporated  $Ti_{1-x}Al_xN$  coatings with increasing Al content," *Surf. Coat. Technol.*, vol. 444, p. 128690, 2022.
35. Y. Moritz, C. Kainz, M. Tkadletz, C. Czettel, M. Pohler, and N. Schalk, "Microstructure and mechanical properties of arc evaporated Ti (Al, Si) N coatings," *Surf. Coat. Technol.*, vol. 421, p. 127461, 2021.
36. R. Daniel, M. Meindlhumer, W. Baumeegger, J. Zalesak, B. Sartory, M. Burghammer, C. Mitterer, and J. Keckes, "Grain boundary design of thin films: using tilted brittle interfaces for multiple crack deflection toughening," *Acta Mater.*, vol. 122, pp. 130–137, 2017.
37. T. Csanádi, M. Vojtko, Z. Dankházi, M. J. Reece, and J. Dusza, "Small scale fracture and strength of high-entropy carbide grains during microcantilever bending experiments," *J. Eur. Ceram. Soc.*, vol. 40, no. 14, pp. 4774–4782, 2020.
38. J. Tatami, M. Katayama, M. Ohnishi, T. Yahagi, T. Takahashi, T. Horiuchi, M. Yokouchi, K. Yasuda, D. K. Kim, T. Wakihara, *et al.*, "Local fracture toughness of  $Si_3N_4$  ceramics measured using single-edge notched microcantilever beam specimens," *J. Am. Ceram. Soc.*, vol. 98, no. 3, pp. 965–971, 2015.
39. J. P. Best, J. Zechner, J. M. Wheeler, R. Schoepner, M. Morstein, and J. Michler, "Small-scale fracture toughness of ceramic thin films: the effects of specimen geometry, ion beam notching and high temperature on chromium nitride toughness evaluation," *Phil. Mag.*, vol. 96, no. 32–34, pp. 3552–3569, 2016.
40. F. Monteverde, S. Guicciardi, and A. Bellosi, "Advances in microstructure and mechanical properties of zirconium diboride based ceramics," *Mater. Sci. Eng. A*, vol. 346, no. 1–2, pp. 310–319, 2003.
41. T. Csanádi, A. Azizpour, M. Vojtko, and W. G. Fahrenholtz, "The effect of crystal anisotropy on fracture toughness and strength of  $ZrB_2$  microcantilevers," *J. Am. Ceram. Soc.*, vol. 107, no. 3, pp. 1669–1681, 2024.
42. M. Vidiš, T. Fiantok, M. Gocník, P. Švec Jr, Š. Nagy, M. Truchlý, V. Izai, T. Roch, L. Satrapinsky, V. Šroba, *et al.*, "Hardness and fracture toughness enhancement in transition metal diboride multilayer films with structural variations," *Materialia*, vol. 34, p. 102070, 2024.
43. C. Hu, S. Lin, M. Podsednik, S. Mráz, T. Wojcik, A. Limbeck, N. Koutná, and P. H. Mayrhofer, "Influence of co-sputtering  $AlB_2$  to  $TaB_2$  on stoichiometry of non-reactively sputtered boride thin films," *Mater. Res. Lett.*, vol. 12, no. 8, pp. 561–570, 2024.
44. T. Glechner, H. Oemer, T. Wojcik, M. Weiss, A. Limbeck, J. Ramm, P. Polcik, and H. Riedl, "Influence of si on the oxidation behavior of tm-si-b2az coatings (tm= ti, cr, hf, ta, w)," *urf. Coat. Technol.*, vol. 434, p. 128178, 2022.
45. C. Fuger, R. Hahn, A. Hirle, T. Wojcik, P. Kutrowatz, F. Bohrn, O. Hunold, P. Polcik, and H. Riedl, "Tissue phase affected fracture toughness of nano-columnar  $TiB_{2+z}$  thin films," *Mater. Res. Lett.*, vol. 11, no. 8, pp. 613–622, 2023.
46. Y. Zhou, H. Xiang, Z. Feng, and Z. Li, "General trends in electronic structure, stability, chemical bonding and mechanical properties of ultrahigh temperature ceramics  $TMB_2$  (TM= transition metal)," *J. Mater. Sci. & technology*, vol. 31, no. 3, pp. 285–294, 2015.
47. Q. Gan, H. Liu, S. Zhang, F. Wang, J. Cheng, X. Wang, S. Dong, Q. Tao, Y. Chen, and P. Zhu, "Robust hydrophobic materials by surface modification in transition-metal diborides," *ACS Appl. Mater. Interfaces*, vol. 13, no. 48, pp. 58162–58169, 2021.
48. W. Sun, H. Xiang, F.-Z. Dai, J. Liu, and Y. Zhou, "Anisotropic surface stability of  $TiB_2$ : A theoretical explanation for the easy grain coarsening," *J. Mater. Res.*, vol. 32, no. 14, pp. 2755–2763, 2017.
49. W. Sun, J. Liu, H. Xiang, and Y. Zhou, "A theoretical investigation on the anisotropic surface stability and oxygen adsorption behavior of  $ZrB_2$ ," *J. Am. Ceram. Soc.*, vol. 99, no. 12, pp. 4113–4120, 2016.
50. T. Yang, X. Han, W. Li, X. Chen, and P. Liu, "First-principles calculations on the interfacial stability and bonding properties of  $HfN(111)/HfB_2(0001)$  interface," *Vacuum*, vol. 207, p. 111678, 2023.
51. C. Hu, S. Mráz, P. J. Pöllmann, T. Wojcik, M. Podsednik, B. Hajas, A. Limbeck, N. Koutná, J. M. Schneider, and P. H. Mayrhofer, "Microstructure, mechanical properties, thermal decomposition and oxidation sequences of crystalline  $AlB_2$  thin films," *Mater. Des.*, vol. 250, p. 113584, 2025.
52. D. Sangiovanni, A. Kjellén, F. Trybel, L. Johnson, M. Odén, F. Tasnádi, and I. Abriksov, "Controlled polymorphic competition—a path to tough and hard ceramics," *arXiv preprint arXiv:2412.15874*, 2024.
53. D. G. Sangiovanni, A. Kraych, M. Mrovec, J. Salamina, M. Odén, F. Tasnádi, and I. A. Abriksov, "Descriptor for slip-induced crack blunting in refractory ceramics," *Phys. Rev. Mater.*, vol. 7, no. 10, p. 103601, 2023.
54. W. Brace, "An extension of the Griffith theory of fracture to rocks," *J. Geophys. Res.*, vol. 65, no. 10, pp. 3477–3480, 1960.
55. M. K. Ferber, P. F. Becher, and C. B. Finch, "Effect of microstructure on the properties of  $TiB_2$  ceramics," *J. Am. Ceram. Soc.*, vol. 66, no. 1, pp. C–2, 1983.

56. S. Bhaumik, C. Divakar, A. K. Singh, and G. Upadhyaya, "Synthesis and sintering of  $TiB_2$  and  $TiB_2$ - $TiC$  composite under high pressure," *Mater. Sci. Eng. A*, vol. 279, no. 1-2, pp. 275–281, 2000.
57. W. Wang, Z. Fu, H. Wang, and R. Yuan, "Influence of hot pressing sintering temperature and time on microstructure and mechanical properties of  $TiB_2$  ceramics," *J. Eur. Ceram. Soc.*, vol. 22, no. 7, pp. 1045–1049, 2002.
58. J. J. Swab, J. Jarman, W. Fahrenholtz, and J. Watts, "Mechanical properties of  $ZrB_2$  ceramics determined by two laboratories," *Int. J. Appl. Ceram. Technol.*, vol. 20, no. 5, pp. 3097–3103, 2023.
59. K. Li, Z. Huang, J. Yuan, X. Li, Z. Wang, M. Hu, T. Wang, X. Hu, Y. Li, and X. Zhang, "Synthesis and growth mechanism of highly crystalized multi-branched  $HfB_2$  micro-rods with self-toughening effect," *Mater. Des.*, vol. 244, p. 113196, 2024.
60. Z. Wang, X. Liu, B. Xu, and Z. Wu, "Fabrication and properties of  $HfB_2$  ceramics based on micron and sub-micron  $HfB_2$  powders synthesized via carbo/borothermal reduction of  $HfO_2$  with  $B_4C$  and carbon," *Int. J. Refract. Met. Hard Mater.*, vol. 51, pp. 130–136, 2015.
61. T. Maccagno and J. Knott, "Brittle fracture under mixed modes I and II loading," *Int. J. Fract.*, vol. 29, pp. R49–R57, 1985.
62. Y. Zhou, J. Wang, Z. Li, X. Zhan, and J. Wang, "First-principles investigation on the chemical bonding and intrinsic elastic properties of transition metal diborides  $TMB_2$  (TM= Zr, Hf, Nb, Ta, and Y)," *Ultra-High Temperature Ceramics: Materials for Extreme Environment Applications*, pp. 60–82, 2014.
63. J. Royer, "Study of pure and mixed-mode fracture of a brittle material," *Exp. Mech.*, vol. 28, pp. 382–387, 1988.
64. M. De Moura, R. Campilho, and J. Gonçalves, "Pure mode II fracture characterization of composite bonded joints," *Int. J. Solids Struct.*, vol. 46, no. 6, pp. 1589–1595, 2009.
65. R. Jalayer, B. Saboori, and M. R. Ayatollahi, "A novel test specimen for mixed mode I/II/III fracture study in brittle materials," *Fatigue Fract. Eng. Mater. Struct.*, vol. 46, no. 5, pp. 1908–1920, 2023.
66. V. Rizov, "Mixed-mode I/II fracture study of polymer composites using single edge notched bend specimens," *Comput. Mater. Sci.*, vol. 77, pp. 1–6, 2013.
67. A. Braham, W. Buttlar, and F. Ni, "Laboratory mixed-mode cracking of asphalt concrete using the single-edge notch beam," *Road Mater. Pavement Des.*, vol. 11, no. 4, pp. 947–968, 2010.
68. R. Margevicius, J. Riedle, and P. Gumbsch, "Fracture toughness of polycrystalline tungsten under mode I and mixed mode I/II loading," *Mater. Sci. Eng. A*, vol. 270, no. 2, pp. 197–209, 1999.
69. I. Gupta, C. Sondergeld, and C. Rai, "Fracture toughness in shales using nano-indentation," *J. Pet. Sci. Eng.*, vol. 191, p. 107222, 2020.
70. B. Hunter, X.-X. Yu, N. De Leon, C. Weinberger, W. Fahrenholtz, G. Hilmas, M. L. Weaver, and G. B. Thompson, "Investigations into the slip behavior of zirconium diboride," *J. Mater. Res.*, vol. 31, no. 18, pp. 2749–2756, 2016.
71. C. Fuger, R. Hahn, L. Zauner, T. Wojcik, M. Weiss, A. Limbeck, O. Hunold, P. Polcik, and H. Riedl, "Anisotropic super-hardness of hexagonal  $WB_{2\pm z}$  thin films," *Mater. Res. Lett.*, vol. 10, no. 2, pp. 70–77, 2022.
72. P. Andric and W. A. Curtin, "Atomistic modeling of fracture," *Model. Simul. Mat. Sci. Eng.*, vol. 27, no. 1, p. 013001, 2018.
73. F. McClintock, "Friction on Griffith cracks in rocks under pressure," in *Proc. 4th US Nat. Congr. Appl. Mech.*, vol. 2, pp. 1015–1022, 1962.
74. G. Kresse and J. Furthmüller, "Efficient iterative schemes for ab initio total-energy calculations using a plane-wave basis set," *Phys. Rev. B*, vol. 54, no. 16, p. 11169, 1996.
75. G. Kresse and D. Joubert, "From ultrasoft pseudopotentials to the projector augmented-wave method," *Phys. Rev. B*, vol. 59, pp. 1758–1775, Jan 1999.
76. J. P. Perdew, A. Ruzsinszky, G. I. Csonka, O. A. Vydrov, G. E. Scuseria, L. A. Constantin, X. Zhou, and K. Burke, "Restoring the density-gradient expansion for exchange in solids and surfaces," *Phys. Rev. Lett.*, vol. 100, p. 136406, Apr 2008.
77. T. Leiner, N. Koutná, J. Janovec, M. Zelený, P. H. Mayrhofer, and D. Holec, "On energetics of allotrope transformations in transition-metal diborides via plane-by-plane shearing," *Vacuum*, vol. 215, p. 112329, 2023.
78. M. Parrinello and A. Rahman, "Polymorphic transitions in single crystals: A new molecular dynamics method," *J. Appl. Phys.*, vol. 52, no. 12, pp. 7182–7190, 1981.
79. D. G. Sangiovanni, F. Tasnádi, T. Harrington, M. Odén, K. S. Vecchio, and I. A. Abrikosov, "Temperature-dependent elastic properties of binary and multicomponent high-entropy refractory carbides," *Mater. Des.*, vol. 204, p. 109634, 2021.
80. A. P. Thompson, H. M. Aktulga, R. Berger, D. S. Bolinteanu, W. M. Brown, P. S. Crozier, P. J. in 't Veld, A. Kohlmeyer, S. G. Moore, T. D. Nguyen, R. Shan, M. J. Stevens, J. Tranchida, C. Trott, and S. J. Plimpton, "LAMMPS - a flexible simulation tool for particle-based materials modeling at the atomic, meso, and continuum scales," *Comp. Phys. Comm.*, vol. 271, p. 108171, 2022.
81. E. V. Podryabinkin and A. V. Shapeev, "Active learning of linearly parametrized interatomic potentials," *Comput. Mater. Sci.*, vol. 140, pp. 171–180, 2017.

82. P. Andric and W. Curtin, “New theory for mode I crack-tip dislocation emission,” *J. Mech. Phys. Solids*, vol. 106, pp. 315–337, 2017.
83. T. C. Ting, *Anisotropic elasticity: theory and applications*, vol. 45. Oxford university press, 1996.
84. M. Schaffer, B. Schaffer, and Q. Ramasse, “Sample preparation for atomic-resolution stem at low voltages by fib,” *Ultramicroscopy*, vol. 114, pp. 62–71, 2012.